

Unveiling the Significant Role on Synthesis of Magnetic CuFe_2O_4 Photocatalyst for Dye Degradation

Is Fatimah^{1,2,*}, Lela Dwi Rahmawati^{1,2}, Nunung Nurlaela^{1,2},
Suresh Sagadevan³, Mohd Rafie Bin Johan³ and Ruey-An Doong⁴

¹Department of Chemistry, Faculty of Mathematics and Natural Sciences, Universitas Islam Indonesia, Daerah Istimewa Yogyakarta 55584, Indonesia

²Nanomaterials and Sustainable Chemistry Research Centre, Universitas Islam Indonesia, Daerah Istimewa Yogyakarta 55584, Indonesia

³Nanotechnology & Catalysis Research Centre, University of Malaya, Kuala Lumpur 50603, Malaysia

⁴Institute of Analytical and Environmental Sciences, National Tsing Hua University, Hsinchu 300044, Taiwan

(*Corresponding author's e-mail: isfatimah@uii.ac.id)

Received: 16 October 2025, Revised: 9 November 2025, Accepted: 16 November 2025, Published: 5 February 2026

Abstract

Metal ferrites have been known and utilized in various applications, including as photocatalyst for organic contaminated water treatment. In this work, exploration on synthesis of copper ferrite (CuFe_2O_4) by evaluating the role of synthesis method and the use of surfactant on physicochemical characteristics has been performed. Effect of hydrothermal (HT) and ultrasound-irradiation methods with and without the addition of cetyltrimethylammonium bromide (CTAB) as templating agent on physical and optical features was analysed using X-ray diffraction (XRD), scanning electron microscopy, Fourier-Transform Infra-red, particle's size analysis, diffuse reflectance UV-Visible spectrophotometry (UV-DRS), and vibrating sample magnetometer (VSM). Photocatalytic activity of the prepared samples was examined in methyl violet photocatalytic degradation under UV and visible lights exposure. The HT treatment produced higher crystallite and particle's size, and the increased size is correlated to decreased band gap energy of nanomaterials. In addition, the particle size which also influenced to magnetism. The band gap energy of materials are ranging at 1.71 - 2.01 eV, while magnetism ranging at 14.45 - 18.41 emu/g with the highest value gained by HT-prepared nanomaterial, while the lowest value is observed by ultrasound-irradiated method. Photocatalytic performance of the prepared materials is excellent as shown by an efficient methyl violet degradation under UV and visible light exposure. The maximum degradation of 99.9% was achieved by CuFe_2O_4 with the lowest band gap and largest crystallite size prepared under hydrothermal method without CTAB addition.

Keywords: Magnetic, Metal ferrite, Photocatalyst, Spinel ferrite

Introduction

In recent years, spinel ferrite magnetic materials have attracted the attention of researchers. Spinel ferrite magnetic materials have unique magnetic, electrical and optical properties and can be applied in various fields [1]. Spinel ferrites are materials with the general formula MFe_2O_4 , where M is a divalent cation such as Zn^{2+} , Ni^{2+} ,

Mn^{2+} , or Cu^{2+} . These materials have received increasing attention in recent years due to their beneficial combination of magnetic, electrical, and optical properties, suitable for a wide range of applications from data storage, biomedical and energy storage [2,3]. Spinel ferrites have shown great potential for environmental

applications such as water treatment agents (heavy metal removal or catalytic destruction of organic pollutants). CuFe_2O_4 is a particle that has an inverse spinel crystal structure. CuFe_2O_4 is one of the spinel ferrites that has been utilized as catalyst and photocatalyst for various reactions. The magnetism of CuFe_2O_4 gives benefit for easy in separation and reusability [4].

Several methods are used for the synthesis of copper ferrite, and these play an important factor to create physicochemical characters for furthermore determine the chemical activity of the material. The methods consist of the sol-gel, mechanochemical method, coprecipitation, microemulsion, hydrothermal method (HT), ultrasound-irradiation (US) and mechanochemical methods. The coprecipitation method is one of the most used methods for synthesis due to its simple and easiness. Additionally, the combination with HT, US or microwave irradiation were applied to intensity the crystallization and particles growth [5]. Similar to some other nanoparticles synthesis, synthesis routes control the physicochemical features of material, including optical properties [6]. In addition, surfactants influence the growth of nanoparticles.

The physicochemical features are theoretically affecting the chemical activity, including optical properties and photocatalytic activity. Considering the magnetic photocatalyst is a required form in dye degradation by photocatalysis mechanisms recently, evaluation on the photocatalytic activity of CuFe_2O_4 is interesting to be explored. Previous works investigated the effect of HT-method and US-method on the morphology, magnetism, optical, crystallite size and infra-red radiance performance [7-9] and study of the effect of cationic surfactant on physicochemical feature of CuFe_2O_4 has been performed [10]. An intensive wavelength and energy supported by US accelerate coprecipitate to the fast nucleation environmentally friendly, safe and inexpensive [11,12]. Particularly, US irradiation leads to faster and more efficient material production, so it is expected to be easily controlled and produce materials that have a specific diameter with a faster rate in the deposition process [2]. However, comparative study on both HT and US methods along with effect of surfactant to the physicochemical character of CuFe_2O_4 nanoparticles for advance

applicability as photocatalyst is not reported yet. Within this scheme, cetyltrimethylammonium bromide (CTAB) is considered as an effective templating agent by the succeed for some nanoparticles synthesis with small concentration required to control nanoparticles growth [13,14]. From these backgrounds, this study is expected to unveil the role of the use of HT method and US irradiation along with the effect of the addition of CTAB in synthesizing CuFe_2O_4 . The comparison of HT and US method and study on the effect surfactant addition to the physicochemical and photocatalytic activity is the novelty of this work which never explored before. The physicochemical characterization was observed is using X-ray diffraction (XRD), Fourier-Transform Infra-Red (FTIR), particle size distribution (PSD), diffuse reflectance UV-Vis Spectrophotometer (UV-DRS), and VSM instruments, while got photocatalytic activity examination, methyl violet was chosen as model of dye molecule. The phenomenon on intensification during nanoparticles formation and was aimed to be studied to get an effective synthesis of CuFe_2O_4 .

Materials and methods

Preparation of CuFe_2O_4

About 4 g of $\text{FeCl}_3 \cdot 6\text{H}_2\text{O}$, 2.72 g of Cu(II) acetate, 2.05 g of sodium acetate and 0.007 g of sodium citrate were mixed with 200 mL of demineralized water. Into the solution, 50 mL of 0.2% of CTAB was added followed by setting up the solution to get pH 10 with the addition of NaOH solution. After furthermore followed by stirring for 1 h, the solution was transferred into a Teflon-lined autoclave, heated at 180 °C overnight. The obtained slurry from these steps was calcined at 500 °C for 2 h, and the sample was encoded as CFO-HTC.

Similar procedure was performed without the addition of CTAB but in HT treatment, and the sample was encoded as CFO-HT. From US treatment, the HT treatment after coprecipitation was replaced by US irradiation to the precipitate for 1 h using commercial ultrasound chamber, and other steps are in same condition. The samples obtained from the synthesis by using CTAB and without CTAB were designated as CFO-S and CFO-

SC. **Figure 1** depicts the scheme of synthesis, and the summary of synthesis conditions is provided in **Table 1**.

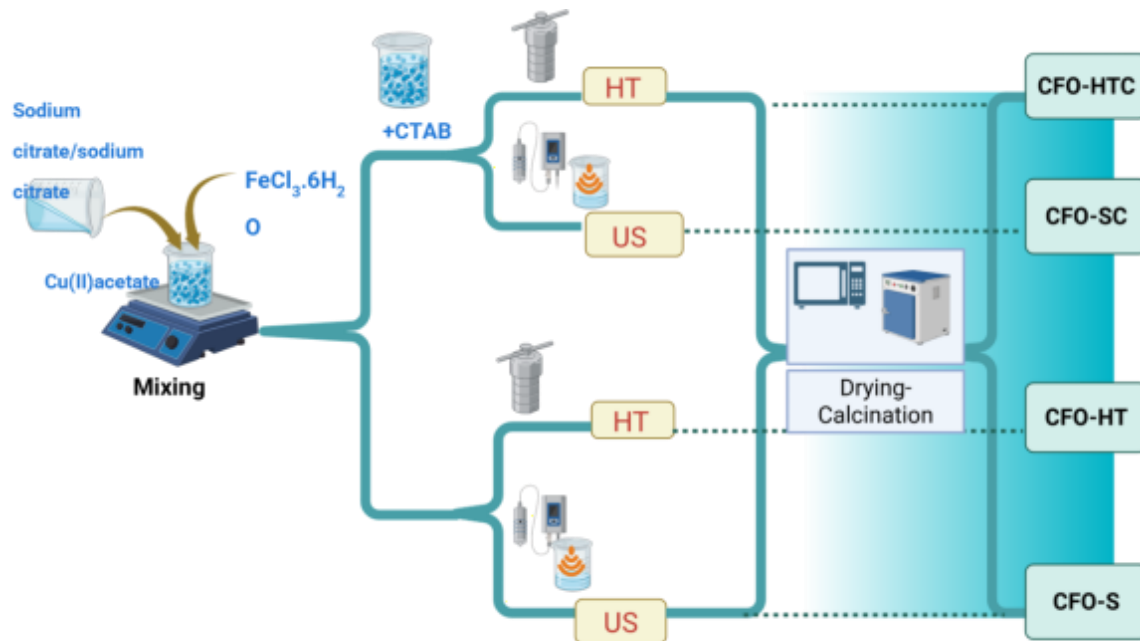


Figure 1 Scheme of synthesis.

Table 1 Resume of samples synthesis condition.

Sample	CTMA 0.2% addition	HT treatment	US treatment
CFO-HTC	+	+	–
CFO-HT	–	+	–
CFO-SC	+	–	+
CFO-S	–	–	+

Material's characterization

The crystallinity and phase of the prepared samples were analysed by using X-ray diffractometer (XRD) spectroscopy on Phenom X³. Ni-filtered Cu K α irradiation ($\lambda = 1.54$) was utilized as photon source, and the measurement was recorded from 10° - 70° of diffraction angles (2θ), step size of 0.1°/step. The morphology of the prepared samples was examined by using field emission scanning electron microscope (FE-SEM). Fourier-transform Infrared Spectroscopy (FT-IR) analysis (Perkin

Elmer Spectrum One, USA) was used to investigate the functional groups in the samples recorded at the 4,000 to 500 cm^{-1} wavelength range. Vibrating magnetometer 7400 Series VSM System (Lake Shore, Ohio) was employed for magnetism analysis, and the hysteresis measurements were performed at 300 K with magnetic field up to 0.9 T to obtain the demagnetisation corrections. Zetta-sizer Nanoseries instrument (Malvern, United Kingdom) was utilized to measure the surface potential of

the samples. UV-DRS of JASCO V760 was used for the band gap energy determination.

Photocatalytic activity examination

The capability of prepared CuFe_2O_4 as photocatalyst was evaluated by batch photocatalytic degradation experiments. Close batch experiments of photocatalytic degradation of methyl violet (MV) were conducted using a reactor equipped with UV lamp (Philips, 20 Watt) with the light intensity of 34.9 W/cm^2 and xenon lamp (Philips, $\lambda = 500 \text{ nm}$, 30 watt) with the light intensity of $32.0 \mu\text{W/cm}^2$ as visible light source. In each experiment, about 0.1 g of the CuFe_2O_4 sample was dispersed into 100 mL of 20 mg/L of MV solution. Stirring for 15 min in a dark condition was performed prior UV light exposure. An aliquot of 5 mL was taken out from that solution after every 15 min, filtered by using syringe filters and then the MV concentration was determined by UV-Visible spectrophotometer (HITACHI U-2080, Japan). Degradation efficiency (DE) was calculated based on the percentage of reduced concentration measured by colorimetric analysis.

Results and discussion

Physicochemical characterization

The XRD diffraction patterns of the prepared sample is presented in **Figure 2**. From the figure, it is seen that all sample show the characteristic peaks of CuFe_2O_4 at 2θ of 16.2° , 33.2° , 35.6° , 38.7° , 49.5° , 54.1° and 62.5° that are in good agreement with the (111), (220), (311), (222), (400), (422), (511) and (440) planes, respectively referred to the Joint Committee on Powder Diffraction (JCPDS) No. 35-0425. In addition, the HT-prepared samples; CFO-HT and CFO-HTC express additional peak at $2\theta = 24.22^\circ$ which potentially demonstrated the presence of Fe_2O_3 . The formation of Fe_2O_3 occurred due to the excess Fe ions in the precursor which accelerate to be hydrated under HT pressure and temperature. Similar phenomenon was obtained in the synthesis of CuFe_2O_4 reported in previous works [15].

Further calculations on crystallite size based on some peaks were performed by following equation Eq. (1), and the results are provided in **Table 2**.

$$D = \frac{K\lambda}{\beta \cos \theta} \quad (1)$$

With K is k is a constant related to the crystalline shape, λ is wavelength, β is full width and half maximum (FWHM), and θ is reflection angle.

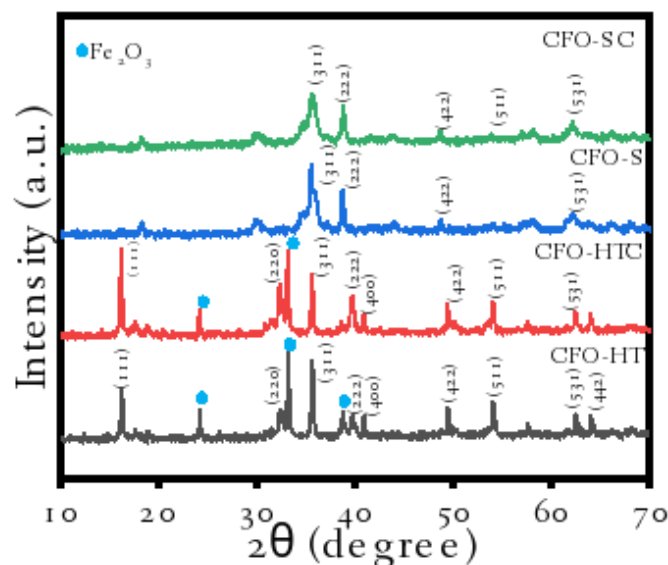


Figure 2 XRD patterns of prepared CuFe_2O_4

Table 2 Calculation of crystallite size based on XRD measurement.

Angle 2θ	CFO-HT		CFO-HTC		CFO-S		CFO-SC	
	FWHM	crystallite size (nm)	FWHM	crystallite size (nm)	FWHM	crystallite size (nm)	FWHM	crystallite size (nm)
16.2°	0.245	32.11	0.216	36.43	0.330	23.77	0.268	29.27
33.2°	0.175	43.52	0.173	44.03	0.679	11.14	0.706	10.87
35.6°	0.223	33.92	0.213	35.52	0.283	26.49	0.747	10.12
38.7°	0.230	32.59	0.394	18.97	0.283	26.49	0.339	22.11
49.5°	0.235	30.71	0.199	36.27	0.315	22.99	0.148	48.94
54.1°	0.266	26.60	0.247	28.66	0.810	8.58	0.228	30.62
62.5°	0.293	23.19	0.305	22.28	0.731	9.31	0.540	12.61
	Mean size = 34.72 nm		Mean size = 33.20 nm		Mean size = 18.40 nm		Mean size = 23.51 nm	

Based on the results obtained in **Table 2**, it is seen that CFO-HT, CFO-HTC, CFO-S and CFO-SC have crystal sizes of 34.72, 33.20, 18.40 and 23.51 nm, respectively. The addition of CTAB into a-HT-synthesized material reduces the crystal size, meanwhile the effect is on opposite way for US-irradiation method. The reduced crystallite size by the presence of the surfactant in the crystal growth is similar to was reported in the synthesis of CuO nanoparticles. The decomposed gel formation of CuO was obtained with the addition of CTAB surfactant and it confirmed the presence of compressive strain in the crystal lattice [16]. Similarly, the addition of Triton-X gave the smaller crystallite size of SnO₂ [17]. The addition of surfactant acted as templating agent to fix the better crystallinity of the particles. As also confirmed by

the FWHM data and available peaks of CuFe₂O₄, the HT-synthesized materials have better crystallinity rather than US-irradiated materials [18]. However, as the energy sufficiently provide faster aggregation of the particles, the surfactant promotes particle's growth for greater size as reported in the use of polyethylene glycol (PEG) in the synthesis of ZnO [19]. Surfactant could increase monodispersion of each reactant to enhance stability of the growth particles. The surfactant concentration modulates the size of nanoparticles due to the hindrance of surfactants and interparticle interaction. Referred to the investigation on effect of surfactants for NiFe₂O₄ and gold nanoparticles syntheses [20,21], mechanism on hindered aggregation is represented in **Figure 3**.

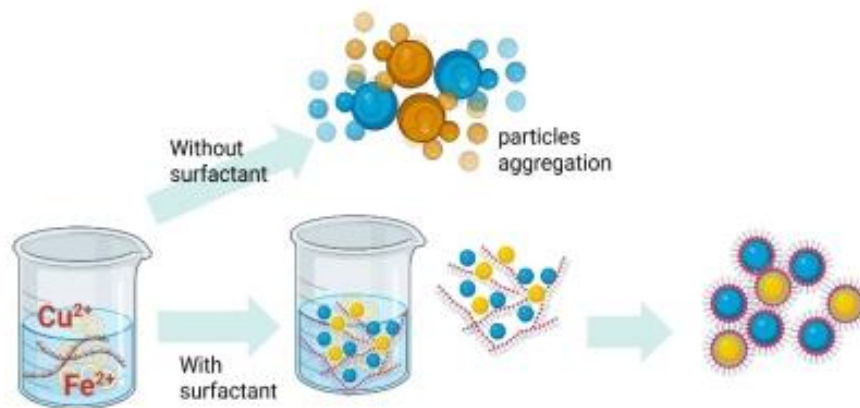


Figure 3 Mechanism of nanoparticles growth by the addition of surfactant.

These data imply that the addition of surfactants consisting of heads (hydrophilic) and tails (hydrophobic) can improve the properties of the synthesized particles. With the presence of surfactants, the surface tension of the solution is reduced so that it can form nucleation and the

formation of new phases. However, in the US- irradiation method, the crystal size does not decrease because the reaction takes place quickly, so that the surfactant does not affect the nucleation process or it influenced to force faster aggregation.

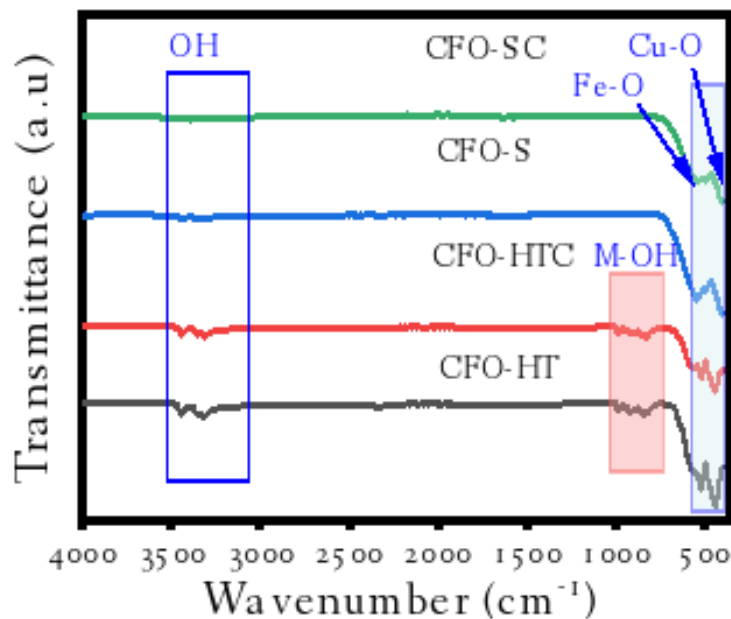


Figure 4 FTIR spectra of materials.

FTIR spectra of the samples (**Figure 4**) show the absorption peaks at around $3,420 - 3,034 \text{ cm}^{-1}$ associated to the peaks at around $1,622 \text{ cm}^{-1}$ refer to water absorption and surface O-H groups in the spectrum of the oxides. In

HT-method synthesized samples (CFO-HT and CFO-HTC), some peaks at around $900 - 800 \text{ cm}^{-1}$ are reflected which are assigned to the the binding of OH with Fe and Cu [22]. In addition, there are some peaks observed at

around 560 cm^{-1} corresponded to the vibrations of the Fe-O bonding and the peaks at around $460 - 475\text{ cm}^{-1}$ revealing the O-Cu binding. The bands are assigned to the

Fe-O tetrahedral group which related to Cu-O demonstrating bond formation between iron and oxygen and copper and oxygen, respectively [23].

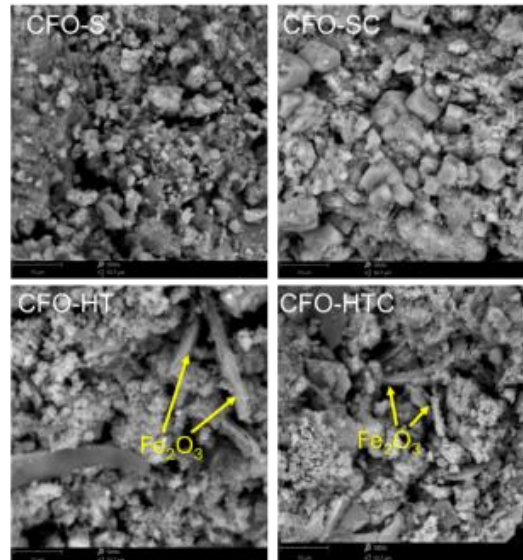


Figure 5 SEM images of prepared materials.

Surface morphology of the prepared samples is expressed irregular forms of the particles, and it is a distinctive surface image presented in **Figure 5**. The hypothesized aggregation is confirmed by the bigger particle's size in CFO-SC compared to other samples. In addition, both CFO-HT and CFO-HTC display the rod-

like forms that are presumable for Fe_2O_3 as also presented from XRD analysis results [24]. Dynamic light scattering (DLS) was used to evaluate the particle's size distribution (PSD) of the prepared materials, and the results are presented in **Figure 6**.

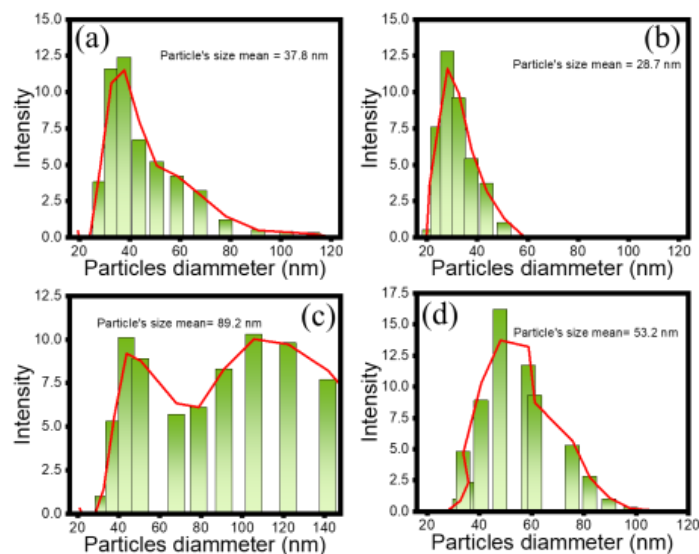


Figure 6 Particle's size distribution of (a) CFO-S, (b) CFO-SC, (c) CFO-HT, and (d) CFO-HTC.

The particle's size of HT-prepared materials demonstrated the larger particle's size compared to coprecipitation method. The faster crystal growth could be provided temperature and pressure in HT condition. In more detail, the addition of CTE reduces the particle's size suggesting the capping agent effect of secondary metabolite of the extract referred to the colloidal stability of crystal growth in the system. Effect of extract concentration influences the colloidal system and sintering to form the particles. This phenomenon was expressed in the formation of SnO_2 and $\text{GdPO}_4 \cdot n\text{H}_2\text{O}$ nanoparticles [25,26].

Magnetic properties

The magnetic properties of the samples were studied using VSM at room temperature, and the hysteresis curves are depicted in **Figure 7**. It can be observed that in general, all samples exhibit ferromagnetic behaviour with magnetism (M_s) and finite coercivity (H_c). The highest magnetism is expressed by CFP-HT with the magnetism of 18.41 emu/g and the less magnetism is observed from CFO-S with 14.45 emu/g. By plotting the relationship

between crystallite size and magnetism, it could be concluded that the magnetism is associated with the larger crystallite size as similar to was reported by the synthesized CuFe_2O_4 using honey mediated sol-gel combustion method [27]. Meanwhile the coercivity is related to the phase anisotropy of tetragonal and hexagonal in spinel ferrite structure. The magnetism values from these are also comparable to was reported as with similar range of crystallite size, the magnetisms area at around 11 - 19 emu/g. Similar range is also considered by the prepared CuFe_2O_4 with crystallite size of 15 nm expressing the magnetism of 11 emu/g [28]. The smaller crystallites generally lead to increase surface effects and disordered layers meanwhile larger crystallites can alter the transition from single domain to multi-domain states, but some other factors such as the morphology of nanoparticles and the presence of other minerals or organic component could influence reduce the magnetism. Thus, the smaller crystallite size influences the magnetic properties for weaker magnetization and higher coercivity [29]. **Table 3** summarizes the crystallite size and magnetism of similar works.

Table 3 Crystallite size and magnetism of prepared CuFe_2O_4 with present work.

Crystallite size (nm)	Magnetism (emu/g)	Reference
14.5 - 22.3	10.2 - 35.4	[28]
43.9	15.4	[30]
17.5	11.66	[31]
20 - 30	31.4	[32]
40 - 50	23.5	[33]
23.51 - 34.72	14.45 - 18.41	This work

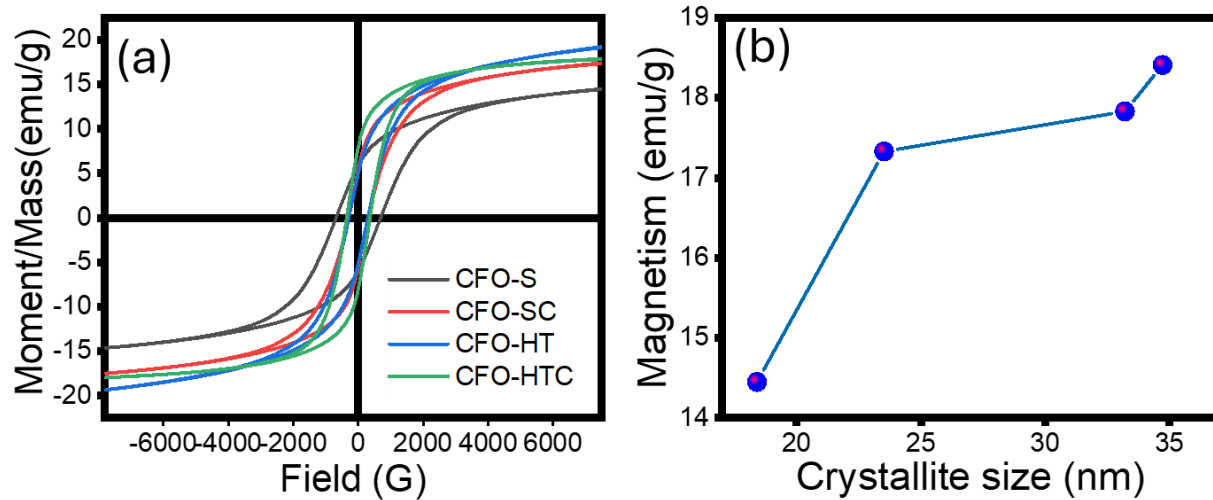


Figure 7 (a) Magnetism of samples and (b) Correlation of crystallite size and magnetism.

Optical properties

The optical property of the prepared materials was evaluated by UV-DRS spectroscopy to determine the band

$$\alpha h\nu = A (h\nu - E_g)^n \quad (2)$$

With α is absorption co-efficient, h is Plank's constant, and θ is the frequency of a photon, with $n = 2$. The E_g values are based on the intrapolation of the graphs between $(\alpha h\nu)^2$ versus $h\nu$ as depicted in **Figure 8**. The calculation gives the E_g values of 2.00, 2.01, 1.71 and 1.81 eV for CFO-S, CFO-SC, CFO-HT and CFO-HTC, respectively. By The smaller crystallite size and higher bandgap energy for NZMF are correlated by the quantum confinement effect. Based on previous research, the crystallite size and particle's size determine the band gap energy as the higher size contributes to reducing the band gap energy. Investigations into CdTe, ZnS, CdSe, ZnSe, and ZnTe nanoparticles revealed that increased particle

gap energy (E_g). Based on the spectra, E_g was calculated using the Tauc's method referred to equation:

size the band gap energy of semiconductor nanomaterials reduces as their particle size increases [34,35].

Investigation resumed the altering optoelectronic properties of InX semiconductor nanoparticles with X = As, Sb, and P significantly dependent on the size and nanoparticles. The blue shifts of optical absorption spectra related to an improved exciton confinement and stronger quantum size effects by smaller nanoparticles. Additionally, morphology and shape of the nanoparticles affect to the density and electronic band structures to change the dynamics and recombination of charge carriers [36]. The correlation between particle's size and band gap energy of prepared samples is plotted in **Figure 8(e)**. The plot tends a non-linear correlation which is similar to was reported from InX nanoparticles and Nano-TiO₂ [37,38].

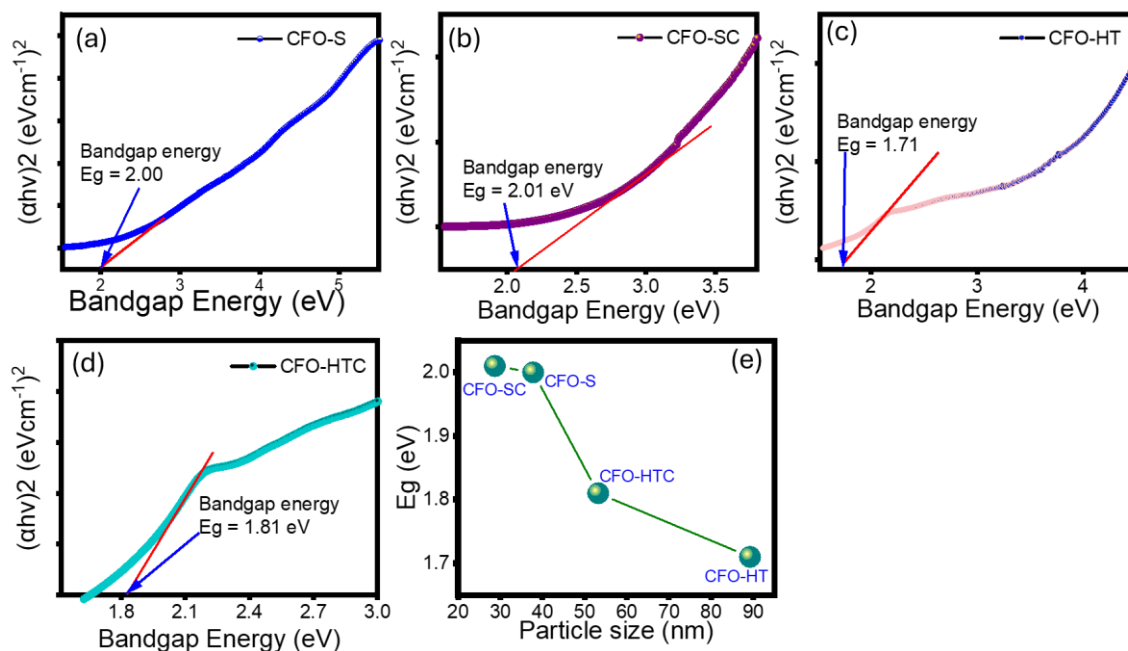


Figure 8 (a) - (d) UV-DRS spectra of prepared materials, (e) Effect of particle's size on E_g .

Photocatalytic activity

The photocatalytic behaviour of the prepared materials was examined on MV degradation on a batch reaction system under UV and visible light exposure. The kinetics evaluation based on concentration change of MV at interval time. The spectral changes of treated MV under UV and visible light are presented in **Figures 7(a) - 7(b)**. Based on the spectral changes, the kinetics plots and the resumed DE are provided in **Figures 7(c) - 7(e)**. There is significant reduced absorbance of the solution by the photocatalytic treatments either by UV or visible light, implying the degradation mechanism of towards MV. The identified degradation is confirmed by the significant difference among the spectral changes and the plots obtained from the photocatalytic treatments respect to the adsorption treatment. Based on the kinetics data, the provided optical properties of all prepared samples are sufficiently supporting the formation of oxidant to degrade MV compound by their interactions with light sources. Based on RE values, it is considered that the activity of the samples is with following order: CFO-HT>CFO-HTC>CFO-S>CFO-SC. The highest photocatalytic

activity achieved by CFO-HT was 99.9%, and it seems that it is in opposite directions with the increased band gap energy. In addition, for all sample, the DE values gained under visible light exposure are higher than that of UV-light exposed treatment.

In this case, the lower band gap energy allows to the faster electron excitation to create radicals for faster oxidation mechanism. Similar phenomenon was observed in the Cu/ZnO composite which the enhanced activity is related to the lowering band gap energy [39]. Similarly, the reduction of band gap of NiSnO₃ and ZnS/TiO₂ causes enhanced optical absorption to facilitate photocatalytic degradation [40,41]. The data suggest that the capability of the samples to absorb photon is suitable with the range of the band gap energy. The higher photoactivity of HT samples could be related to the presence of Fe₂O₃. As byproduct or impurity of the synthesis, the combination of small amount Fe₂O₃ with CuFe₂O₄ could support the photocatalytic mechanism via Z-scheme as also reported by previous works [42,43]. The proposed scheme is presented in **Figure 9**.

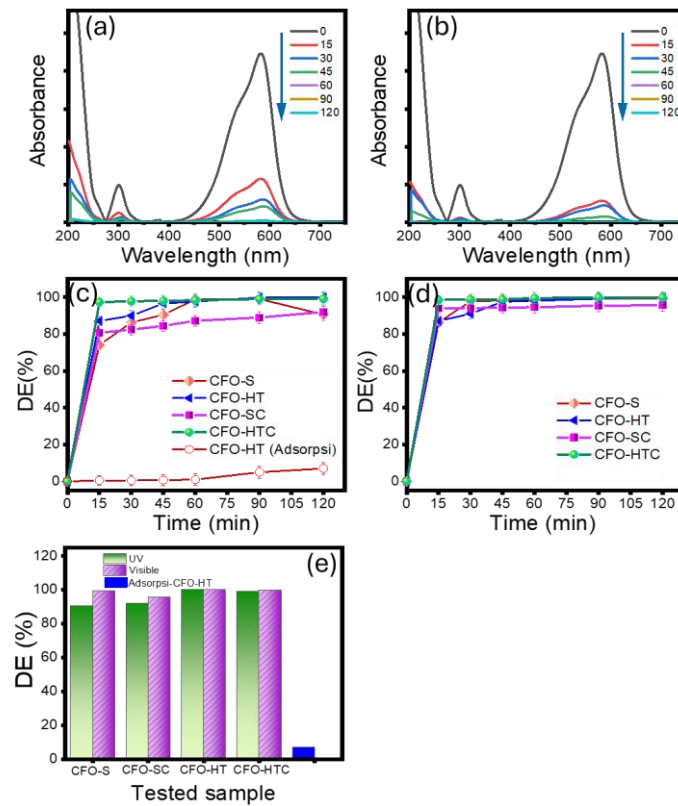


Figure 9 (a) and (b) Spectral changes of treated MV using CFO-HT under UV and visible light, respectively, (c) and (d) Kinetics plots of MV degradation using prepared samples under UV and visible light, e. Resumed DE gained by treatment on the prepared samples.

Based on kinetics data, the photocatalytic degradation of MV obeys first-order kinetic model theory expressed by equation:

$$\ln \frac{C_0}{C_t} = kt \quad (3)$$

where k represents reaction rate constant (min^{-1}), C_0 and C_t are the concentrations of MV at initial and at reaction time of t . The plots and calculated k values referred to the equation are presented in **Figure 10**. Resumed DE and k values for each process using prepared materials are presented in **Table 4**.

Table 4 Recapitulated DE and k values of the treatments using prepared materials.

Sample	Photocatalytic treatment using UV light		Photocatalytic treatment using visible light	
	DE (%)	k (min^{-1})	DE (%)	k (min^{-1})
CFO-HTC	99.1	1.29×10^{-2}	99.83	5.00×10^{-2}
CFO-HT	99.9	5.60×10^{-2}	99.90	3.83×10^{-2}
CFO-SC	91.96	5.13×10^{-3}	95.60	3.77×10^{-3}
CFO-S	90.58	4.70×10^{-3}	99.23	3.00×10^{-2}

The values evidence and in accordance with the performance of materials. In general, all DE data represents a comparable activity to similar materials were reported by previous works as listed in **Table 5**. In

addition, the fitness of MV degradation reaction to the pseudo-first order kinetics is summarized from all listed works.

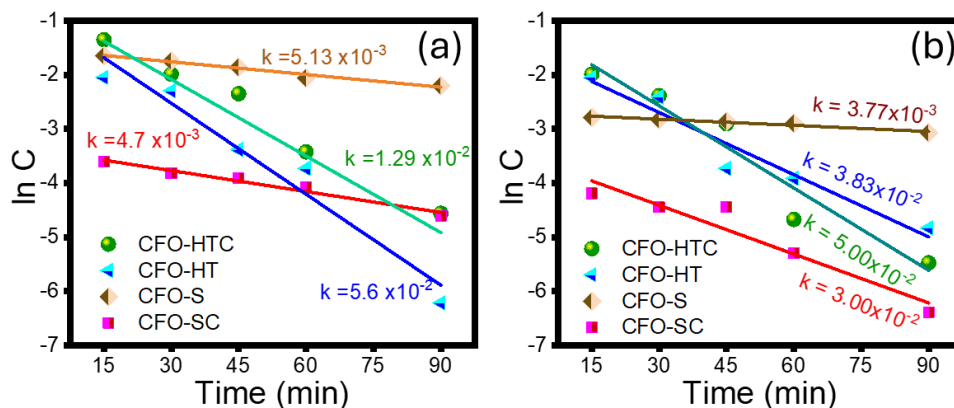


Figure 10 Pseudo-first order plots of MV degradation using prepared samples using (a) UV light and (b) visible light.

Table 5 Comparison on photocatalytic activity of CuFe_2O_4 and related materials for MV degradation.

Sample	Remark	DE (%)	Reference
CuFe_2O_4	The prepared CuFe_2O_4 has a band gap energy of 1.8 eV. The DE applied for 15 mg/L of MV was 98% by treatment under halogen lamp ($\lambda > 400$ nm)	98	[44]
CuFe_2O_4 and $\text{CuFe}_2\text{O}_4/\text{clays}$	A degradation efficiency of 78% was gained by the material for MV degradation for 60 min under UV light illumination. The increased degradation was achieved by combination in $\text{CuFe}_2\text{O}_4/\text{clay}$.	78 and 98	[45]
$\text{CuFe}_2\text{O}_4@\text{CeO}_2$	$\text{CuFe}_2\text{O}_4@\text{CeO}_2$ nanocomposite shows an excellent MV degradation rate of 95.35% under visible-light irradiation within 1.5 h	95.35	[46]
CuFe_2O_4 and Ag- CuFe_2O_4	The degradation efficiency for MV by was 60% and 82.7%, respectively. The reaction was applied for 8 ppm of MV under visible light for 160 min	60 and 82.7	[47]
CuFe_2O_4	The nanomaterial was prepared using HT-assisted method and utilizing CTAB as surfactant. The band gap energy of material is 1.71 eV.	99.9	This work

Mechanism of photocatalysis

It has been discussed elsewhere that the photocatalyst play role to create the radicals as the surface absorb energy from light. The sufficient energy from

photon leads to electron excitation and the formation of hole (h^+). The interaction among h^+ and OH^- creates radicals which furthermore, by interactions with O_2 could form superoxide radicals $\bullet\text{OOH}$. From the excited

electron, the interaction of surface with O_2 could produce can produce superoxide radicals ($\bullet O_2^-$). The oxidation potential of these species is the main reactant for dye degradation. To investigate the contributing species in the dye degradation mechanism, kinetics evaluation of the reaction by the addition of scavengers was performed. Isopropanol (IPR), EDTA and BQ were employed as OH , h^+ and OOH scavengers, respectively. The chart provided in **Figure 11** suggests that the addition of IPR is the most influential scavenger to inhibit the reaction, followed by BQ and EDTA. This implies that the excitation of electron plays the most important role for creating oxidant. Furthermore, the created radicals propagate the formation of other oxidant species, referred to following mechanism:

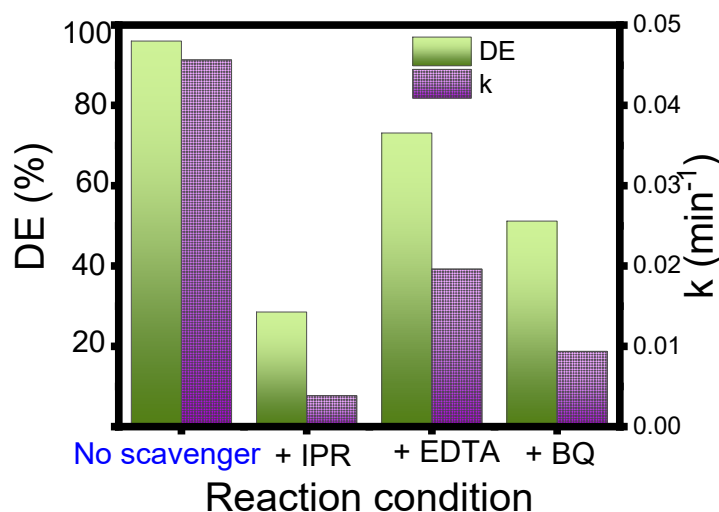
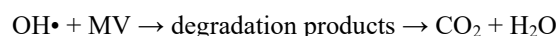
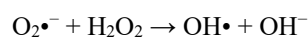
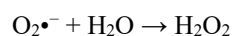
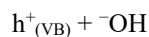
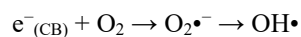


Figure 11 Effect of scavengers on DE and kinetics constant.

Conclusions

This study provides a detailed analysis on effect of hydrothermal and ultrasound-irradiation procedures in the synthesis of $CuFe_2O_4$. The results indicate that the synthesis route affected the crystallite size, magnetism, and band gap energy of the nanoparticles. The presence of CTAB surfactant and templating agent governs the crystallite growth, which also depends on the temperature and pressure of the crystallization. This impact to different effect on crystallization under ultrasound-irradiation and hydrothermal condition. The increased crystallite size led

to the enhanced magnetism and higher band gap energy. Moreover, the lower band gap energy determines as an important factor to increase photocatalytic activity. An excellent photocatalytic activity was expressed by the high efficiency towards methyl violet degradation. Maximum degradation efficiency of 99.9% was achieved on 120 min photocatalytic treatment under visible light on $CuFe_2O_4$ prepared under hydrothermal synthesis without CTAB addition.

Declaration of Generative AI in Scientific Writing

There is no AI tools used for research and manuscript preparation.

CRedit Author Statement

Is Fatimah: Conceptualization; Methodology; Software. **Lela Dwi Rahmawati:** Data curation; Writing - Original draft preparation. **Nunung Nurlaela:** Data curation; Writing - Original draft preparation. **Suresh Sagadevan:** Visualization; Investigation. **Mohd Rafie bin Johan:** Supervision- Reviewing and Editing. **Ruey-an Doong:** Methodology- Data Curation-Reviewing and Editing.

References

- [1] JR la Calvo-De and M Segarra. Optimization of the synthesis of copper ferrite nanoparticles by a polymer-assisted sol-gel method. *ACS Omega* 2019; **4(19)**, 18289-18298.
- [2] FH Mulud, NA Dahham and IF Waheed. Synthesis and characterization of copper ferrite nanoparticles. *IOP Conference Series: Materials Science and Engineering* 2020; **928**, 072125.
- [3] MQ Fahem, MH Jawad, RO Abdulsada and ZT Turki. The structure and electrical properties of NiFe₂O₄ and NiMgFe₂O₄ prepared via sol-gel method. *Ionics* 2024; **31**, 6475-6481.
- [4] SP Keerthana, R Yuvakkumar, G Ravi, S Pavithra, M Thambidurai, C Dang and D Velauthapillai. Pure and Ce-doped spinel CuFe₂O₄ photocatalysts for efficient rhodamine B degradation. *Environmental Research* 2021; **200**, 111528.
- [5] MH Jawad, AA Assi and AM Hameed. Hydrothermal synthesis of zinc oxide nanostructures using varied reactor designs: A comparative study. *Plasmonic* 2025; **20**, 7883-7894.
- [6] G Nabiyouni, D Ghanbari, A Yousofnejad, M Seraj and Z Mirdamadian. Microwave-Assisted synthesis of CuFe₂O₄ nanoparticles and Starch-Based magnetic nanocomposites. *Journal of Nanostructures* 2013; **3(2)**, 155-160.
- [7] H Hou, G Xu, S Tan and S Xiang. A facile hydrothermal synthesis of nanoscale CuFe₂O₄ spinels with enhanced infrared radiation performance. *Journal of Alloys and Compounds* 2018; **735**, 2205-2211.
- [8] U Naresh, RJ Kumar and T Ram. Optical properties of copper ferrite nano-particle synthesized via hydrothermal technique. *Bulletin of Pure & Applied Sciences- Physics* 2018; **37(2)**, 172.
- [9] T Ramesh, V Madhavi, PV Rao, K Vagdevi, N Basavegowda and KH Baek. Impact of ultrasonic-assisted co-precipitation synthesis and ultrasonication duration on cobalt ferrite nanostructures: A comparative study of structural, morphological, optical and magnetic properties. *Inorganic Chemistry Communications* 2025; **174(1)**, 114035.
- [10] P Paramasivan and P Venkatesh. Controllable synthesis of CuFe₂O₄ nanostructures through simple hydrothermal method in the presence of thioglycolic acid. *Physica E: Low-Dimensional Systems and Nanostructures* 2016; **84**, 258-262.
- [11] AR Abbasian, SS Hosseini, M Shayesteh, MS Afarani and MR Esmailzadei. Ultrasonic-assisted solvothermal synthesis of self-assembled Copper Ferrite nanoparticles. *International Journal of Nano Dimension* 2020; **11(2)**, 130-144.
- [12] SF Rus, P Vlazan, S Novaconi, P Sfirloaga and I Grozescu. Synthesis and characterization CuFe₂O₄ nanoparticles prepared by the hydrothermal ultrasonic assisted method. *Journal of Optoelectronics and Advanced Materials* 2012; **14(3)**, 293-297.
- [13] A Memar, CM Phan and MO Tade. Influence of surfactants on Fe₂O₃ nanostructure photoanode. *International Journal of Hydrogen Energy* 2012; **37(22)**, 16835-16843.
- [14] AS Patil, RT Patil and VJ Fulari. Surfactant assisted synthesis of CuO nanostructures for nonenzymatic glucose sensor. *Materials Today: Proceedings* 2021; **46(6)**, 2340-2346.
- [15] KW Jeon, JW Park, RR Lee, JH Gong, WJ Jang, JO Shim and YW Ju. Facile synthesis of CuFe₂O₄ catalyst by the electrospinning method to produce hydrogen via the water gas shift of waste-derived

- syngas. *Journal of Environmental Chemical Engineering* 2023; **11(3)**, 110105.
- [16] I Singh and RK Bedi. Surfactant-assisted synthesis, characterizations, and room temperature ammonia sensing mechanism of nanocrystalline CuO. *Solid State Sciences* 2011; **13(11)**, 2011-2018.
- [17] S Karuppiyah, S Thangaraj, SA Palaniappan and SO Lakshmanan. Influence of surfactants on structural, morphological, optical and antibacterial properties of SnO₂ nanoparticles. *IET Nanobiotechnology* 2019; **13(9)**, 952-956.
- [18] H Liu, S Ji, H Yang, H Zhang and M Tang. Ultrasonic-assisted ultra-rapid synthesis of monodisperse meso-SiO₂@Fe₃O₄ microspheres with enhanced mesoporous structure. *Ultrasonics Sonochemistry* 2014; **21(2)**, 505-512.
- [19] CC Vidyasagar and YA Naik. Surfactant (PEG 400) effects on crystallinity of ZnO nanoparticles. *Arabian Journal of Chemistry* 2016; **9(4)**, 507-510.
- [20] RS López, VF Puentes, NG Bastús, C Hervés and C Jaime. Nucleation and growth of gold nanoparticles in the presence of different surfactants. A dissipative particle dynamics study. *Scientific Reports* 2022; **12**, 13926.
- [21] RS Babu, E Madai, DS Nair, P Gonugunta, SM Armaki, R Hendrikx, T Panneerselvam, R Murugan, VVRK Kumar, P Taheri, A Mol, N Satyanarayana and PR Anusuyadevi. Effect of synthesis conditions on morphology, surface chemistry and electrochemical performance of nickel ferrite nanoparticles for lithium - ion battery applications. *Journal of Materials Science: Materials in Electronics* 2025; **36**, 865.
- [22] M Sharma, G Sharma, N Tyagi, AM Siddiqui and M Khanuja. Advanced photocatalytic degradation of textile dyes and removal of heavy metal ions from MFe₂O₄ using photo-Fenton mechanism. *Journal of Materials Science: Materials in Electronics* 2024; **35**, 497.
- [23] A Meidanchi and H Ansari. Copper spinel ferrite superparamagnetic nanoparticles as a novel radiotherapy enhancer effect in cancer treatment. *Journal of Cluster Science* 2020; **32**, 657-663.
- [24] B Ghalib and M Hessien. Magnetic and antibacterial properties of substituted cobalt spinel ferrite nanocomposites synthesized via henna green microwave hydrothermal method. *Scientific Reports* 2025; **15**, 16653.
- [25] I Fatimah, G Purwiandono, MH Jauhari, AAAP Maharani, S Sagadevan, WC Oh and RA Doong. Synthesis and control of the morphology of SnO₂ nanoparticles via various concentrations of *Tinospora cordifolia* stem extract and reduction methods. *Arabian Journal of Chemistry* 2022; **15(4)**, 103738.
- [26] M Janulevicius, V Klimkevicius, A Vanetsev, V Plausinaitiene, S Sakirzanovas and A Katelnikovas. Controlled hydrothermal synthesis, morphological design and colloidal stability of GdPO₄·nH₂O particles. *Materials Today Communications* 2020; **23**, 100934.
- [27] RS Yadav, I Kuřitka, J Vilcakova, J Havlica, J Masilko, L Kalina, J Tkacz, M Hajdúchová and V Enev. Structural, dielectric, electrical and magnetic properties of CuFe₂O₄ nanoparticles synthesized by honey mediated sol-gel combustion method and annealing effect. *Journal of Materials Science: Materials in Electronics* 2017; **28**, 6245-6261.
- [28] MK Satheeshkumar, ER Kumar, C Srinivas, G Prasad, SS Meena, I Pradeep, N Suriyanarayanan and DL Sastry. Structural and magnetic properties of CuFe₂O₄ ferrite nanoparticles synthesized by cow urine assisted combustion method. *Journal of Magnetism and Magnetic Materials* 2019; **484**, 120-125.
- [29] X Wang, M Zhu, LK Koopal, W Li, W Xu, F Liu, J Zhang, Q Liu, X Feng and DL Sparks. Effects of crystallite size on the structure and magnetism of ferrihydrite. *Environmental Science Nano* 2016; **3(1)**, 190-202.
- [30] TR Neves, LFL Schildt, MLLSE Silva, VVV Vasconcelos, CD Conzo, F Mura, M Rossi, G Varvaro, M Abdolrahimi, S Quaranta, SAD Ferreira and EC Paris. Magnetic CuFe₂O₄ nanoparticles immobilized on modified rice husk-derived zeolite for chlorogenic acid adsorption. *Magnetochemistry* 2024; **10(11)**, 87.
- [31] S Anandan, T Selvamani, G Guru Prasad, AM Asiri and JJ Wu. Magnetic and catalytic properties of inverse spinel CuFe₂O₄ nanoparticles. *Journal of*

- Magnetism and Magnetic Materials* 2017; **432**, 437-443.
- [32] M Awad and I Zhitomirsky. Magnetic CuFe₂O₄ spinel-polypyrrole pseudocapacitive composites for energy storage. *Materials* 2024; **17(21)**, 5249.
- [33] S Singhal, T Namgyal, N Laxhmi and S Bansal. Doping assisted structural transition in copper substituted MgFe₂O₄ ferrite: Thermal, electrical and magnetic properties. *Scientia Iranica* 2013; **20(6)**, 2323-2331.
- [34] M Singh and A Singhal. Modeling of shape and size effects for the band gap of semiconductor nanoparticles. In: Proceedings of the 2018 2nd International Conference on Micro-Electronics and Telecommunication Engineering (ICMETE), Ghaziabad, India. 2018, p. 339-342.
- [35] HV Ganvir, B Jonathan, KS Kumar, VP Raju, K Prabhakaran and NP Hegde. Validation of size of semiconductor nano material: Effect on size and shape. *Communication on Applied Nonlinear Analysis* 2025; **32(2)**, 113-122.
- [36] GT Sherka and HD Berry. Insight into impact of size and shape on optoelectronic properties of InX (X = As, Sb, and P) semiconductor nanoparticles: A theoretical study. *Frontiers in Physics* 2024; **12**, 1447997.
- [37] M Singh, M Goyal and K Devlal. Size and shape effects on the band gap of semiconductor compound nanomaterials. *Journal of Taibah University for Science* 2018; **12(4)**, 470-475.
- [38] A Gautam, K As, S Banerjee, D Vv and K Pk. UVC-Shielding by Nano-TiO₂/PMMA composite: A chemical approach. *Journal of Materials Science & Nanotechnology* 2016; **4(1)**, 105.
- [39] A Modwi, MA Ghanem, AM Al-Mayouf and A Houas. Lowering energy band gap and enhancing photocatalytic properties of Cu/ZnO composite decorated by transition metals. *Journal of Molecular Structure* 2018; **1173**, 1-6.
- [40] M Khatun, P Mitra and S Mukherjee. Effect of band gap and particle size on photocatalytic degradation of NiSnO₃ nanopowder for some conventional organic dyes. *Hybrid Advances* 2023; **4**, 100079.
- [41] S Khosravi, N Chaibakhsh, S Jafari and M Nilkar. Enhanced photocatalytic activity of ZnS/TiO₂ nanocomposite by nitrogen and tetrafluoromethane plasma treatments. *Scientific Reports* 2024; **14(1)**, 28385.
- [42] S Hussain, S Hussain, A Waleed, MM Tavakoli, Z Wang, S Yang, Z Fan and MA Nadeem. Fabrication of CuFe₂O₄/α-Fe₂O₃ composite thin films on FTO Coated Glass and 3-D Nanospire structures for efficient photoelectrochemical water splitting. *ACS Applied Materials & Interfaces Journal* 2016; **8(51)**, 35315-35322.
- [43] A Alneha, M Hadi, H Alnahari and A Al-Sharabi. Optical, structural and antibacterial properties of phase heterostructured nanocomposite. *Scientific Reports* 2024; **14(1)**, 14392.
- [44] A Aslam, MZ Abid, K Rafiq, A Rauf and E Hussain. Tunable sulphur doping on CuFe₂O₄ nanostructures for the selective elimination of organic dyes from water. *Scientific Reports* 2023; **13(1)**, 6306.
- [45] H Madhu and S Rajendra. Green synthesis and reflux method of CuFe₂O₄ and Clay/CuFe₂O₄ nanocomposite for photocatalysis and antioxidant studies. *Chemistry of Inorganic Materials* 2025; **6**, 100099.
- [46] F Touahra, S Zemmache, S Djema, R Chebout, D Lerari and K Bachari. A new approach to the synthesis of CuFe₂O₄@CeO₂ direct Z-scheme with a core-shell structure for enhanced photo-degradation of methyl violet under ultraviolet and visible-light irradiation. *Environmental Progress and Sustainable Energy* 2022; **41(5)**, 13865.
- [47] FMA Alzahrani, J Arshad, MS Al-Buriahi, ZA Alrowaili and S Munir. Synthesis of graphene-based Ag-doped CuFe₂O₄ composite for improved photocatalytic activity against industrial effluents. *Journal of Taibah University for Science* 2023; **17(1)**, 2209676.